ADVANCED OPTICAL MATERIALS
www.advopticalmat.de

Materials Views
www.MaterialsViews.com

Electrically Reconfigurable Metasurfaces Using Heterojunction Resonators

*Prasad P. Iyer, Mihir Pendharkar, and Jon A. Schuller**

An electrically reconfigurable metasurface comprising an array of 1D semiconductor Mie resonators on a reflecting ground plane is theoretically demonstrated. The design is based on magnetic dipole modes that interfere with image fields in a metal substrate to produce a 2π phase shift in reflection about the resonance wavelength. Analogous voltage-dependent phase shifts are produced using novel InSb/$In_{0.8}Al_{0.2}Sb$ heterojunction resonators incorporating top electrodes that minimize perturbations of the electromagnetic mode. The devices exploit large swings in the InSb electron density to produce mid-infrared resonances tunable through free carrier refraction. Combined electrical device and full wave electromagnetic simulations show up to 300° phase shifts with less than 1dB of loss. Using this resonator as a basic building block, an electrically tunable metasurface is demonstrated. By applying a voltage gradient across the metasurface, an incident beam is steered in a unidirectional fashion continuously between ±72° (from normal incidence. This work describes a pathway to unprecedented control of light via electrically reconfigurable metasurfaces.

1. Introduction

The ability to control light-matter interactions at subwavelength scales using engineered structures has enabled the recent surge in metasurface research.[1–5] Using metasurfaces, researchers achieve control over the phase,[6,7] amplitude,[8,9] and polarization[10,11] of light by designing phased arrays of subwavelength resonator elements. These arrays can effect the functions of traditional optical elements by producing the appropriate spatial phase profile.[12] Such metasurfaces have thus been used as flat optical elements,[4,13,14] ultrathin light absorbers,[15–17] and optical sensors,[14,18–20] to name a few applications. In general, metasurfaces exploit the ability to engineer the phase of light between 0 and 2π at subwavelength scales to form arbitrary wave fronts[21,22] that reproduce the behavior of refractive and diffractive optical elements. To date, researchers have performed this phase engineering by changing the physical geometry or shape of resonators, producing static metasurfaces.[2] The ability to dynamically tune the phase of light between 0 and 2π at subwavelength scales would thus promise a new paradigm in reconfigurable metasurface-based optics. Here, we use electromagnetics and device simulations to design electrically pumped semiconductor heterostructure resonators capable of arbitrarily tuning the reflection phase of infrared light with little change in amplitude.

Previous approaches for tuning metasurfaces—using metallic resonators coupled to an index tunable background[8,23–28] or mechanically changing the shape of metallic resonators[5,29,30] have been unable to achieve reconfigurable 2π phase shifts. This inability to achieve 2π phase control stems fundamentally from the nature of the underlying optical antennas. Because the light-matter interaction lengths are subwavelength and the quality factors modest ($Q \approx 1$–10), very large refractive index modulation is needed ($\Delta n \geq 1$). InSb[31–33] or InAs[27,34,35] support free-carrier index shifts of this magnitude due to their high mobility and low electron effective mass. In our previous theory work,[36] we demonstrated full 2π tuning of the transmission phase of semiconductor metasurface by modulating the carrier concentration in InSb resonators between 10^{17}–10^{18} cm^{-3}. However, we did not consider how to achieve such modulation. Here, we use combined electromagnetic[37] and device simulations to demonstrate subwavelength 1D heterojunction device resonators with electrically reconfigurable reflection phase. We first demonstrate a new resonator geometry that allows for integration of metal electrodes with dielectric-type Mie resonances. Subsequently, we incorporate an InSb based heterojunction device layer into the resonator architecture. This novel device design employs electron and hole blocking layers to achieve large modulations of carrier concentration over electrically large dimensions, enabling near-2π tuning of reflection phase with minimal changes in reflection amplitude. Finally, we demonstrate fully continuous and tunable steering of high-quality narrow, diffraction lobes in resonator arrays.

P. P. Iyer, M. Pendharkar, Prof. J. A. Schuller
Electrical and Computer Engineering Department
University of California Santa Barbara
Santa Barbara, CA 93106, USA
E-mail: jonschuller@ece.ucsb.edu

DOI: 10.1002/adom.201600297

2. Results and Discussion

Given the need for integrating top and bottom electrical contacts, our basic metasurface element is a modified version of a 1D "strip" resonator sitting atop a reflecting back electrode shown in **Figure 1**A. The resonances of individual or periodic

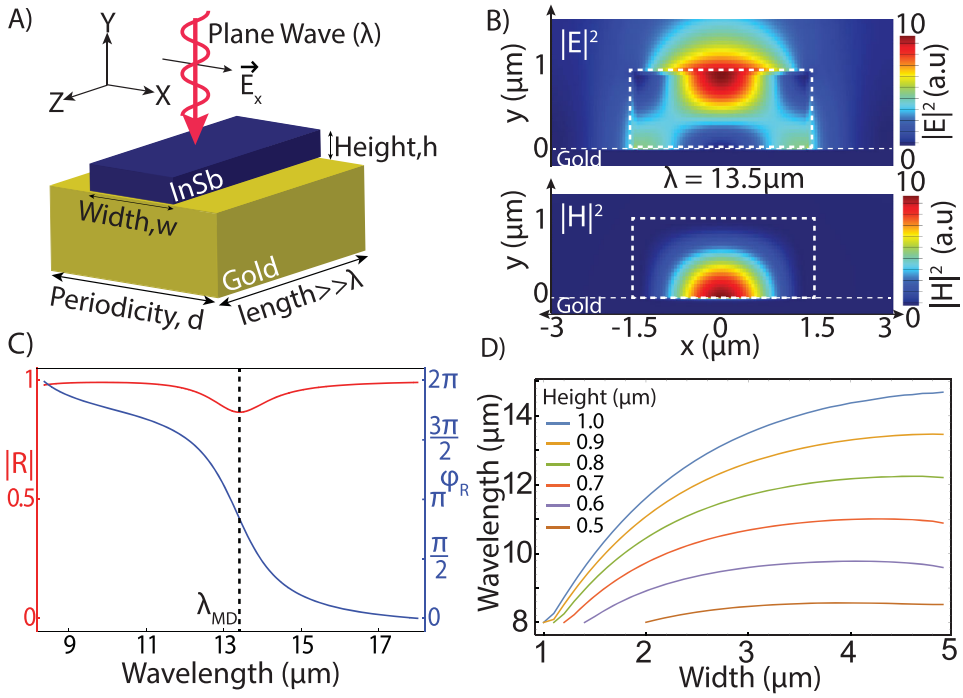

Figure 1. A) Sketch showing the dielectric (InSb) wire grating of width w, height h, and periodicity d, on a metal (Au) substrate illuminated with linearly (TM, x) polarized light at normal incidence. B) Electric (top) and magnetic (bottom) field intensity profiles of the fundamental magnetic dipole resonance excited within the resonator ($w = 3$ μm, $h = 1$ μm, and $d = 6$ μm) structure at an incident wavelength of 13.5 μm. The white dashed outline shows the boundaries within a single unit cell of the periodic structure. C) Reflection amplitude (red axis on left) and phase (blue axis on right) as a function of the incident wavelength. The dashed line indicates the resonant wavelength λ_{MD}. The reflection coefficient goes through a 2π phase shift around this resonance. D) Dispersion of the fundamental magnetic dipole resonance wavelength as a function of width for different height resonators ($d = 6$ μm). The curves flatten beyond ≈3 μm widths as a result of the localization of the electromagnetic intensity to the middle of the resonator.

arrays of such structures can be deconstructed based on the perturbed Mie resonances in an infinite dielectric cylinder.[15,38–42] For transverse magnetic (TM, *E*-field along the *x*-axis) polarized plane-wave illumination the fundamental resonance is a magnetic dipole-like mode. On resonance, the electric field intensity is concentrated near the top of the resonator (Figure 1B). The interaction of the top electric field with its image creates an effective current loop, producing resonant magnetic fields centered at the substrate interface and pointing along the long axis of the resonator (*z*-axis). At the magnetic dipole resonance wavelength (λ_{MD}), these electric and magnetic field intensities are maximized. Of greater interest, however, is the impact of these resonances on the reflection amplitude and phase.

The reflection amplitude (red) and phase (blue) of a wire resonator array near the MD resonance is plotted in Figure 1C. The MD resonance, centered at 13.5 μm, leads to a 2π phase shift as the wavelength varies between 10 to 16 μm. Ordinarily, a single scattering resonance (electric[39] or magnetic[38]) can at most shift the phase of light by π radians.[43] Placing resonators on a metal substrate, however, gives a full 2π phase shift due to interference with image modes in the substrate.[44] Unlike metallic resonators, these dielectric resonators have negligible losses (imaginary part of refractive index $\approx 10^{-3}$). As a result, the reflection has a near unity amplitude at all wavelengths, an ideal characteristic for a reflect array metasurface. The resonance wavelength can be identified from small dips in the reflection amplitude, or by the wavelength of maximum phase gradient ($\partial\phi/\partial\lambda$) (Supporting Information). We exploit this fact to determine the dispersion of resonance wavelengths with resonator geometry in order to identify an optimal design for phase tunability.

The resonance wavelengths can be tuned from 8 to 15 μm by geometrically varying the size and aspect ratio of strip resonators. In Figure 1D, we plot the dispersion of the MD resonance as a function of width (w) for different heights (h). At smaller widths ($w < 2$ μm), the resonance wavelength is more sensitive to changes in width than height, i.e., $\frac{\partial\lambda_{MD}}{\partial w} > \frac{\partial\lambda_{MD}}{\partial h}$. At larger widths ($w > 3$ μm), the curves flatten and the opposite is true, i.e., $\frac{\partial\lambda_{MD}}{\partial h} > \frac{\partial\lambda_{MD}}{\partial w}$. This relative insensitivity to changes in width arises from the localization of the electric field intensity to the center of the resonator (Figure 1B). Our design ultimately requires sufficient width to incorporate metallic electrodes in these side regions of low E-field intensity; throughout this paper we use 3 μm wide resonators. Since introducing free-carriers causes a resonance blueshift,[36] we design the initial resonance wavelength (13.5 μm) red shifted with respect to the operating wavelength (11.35 μm) by selecting a resonator height of 1 μm.

As seen in Figure 1B, the electric field intensity is localized near the top of the resonator. In designing a free carrier-tunable resonator, one only needs to change the carrier concentration in this region of the resonator. Previous work using

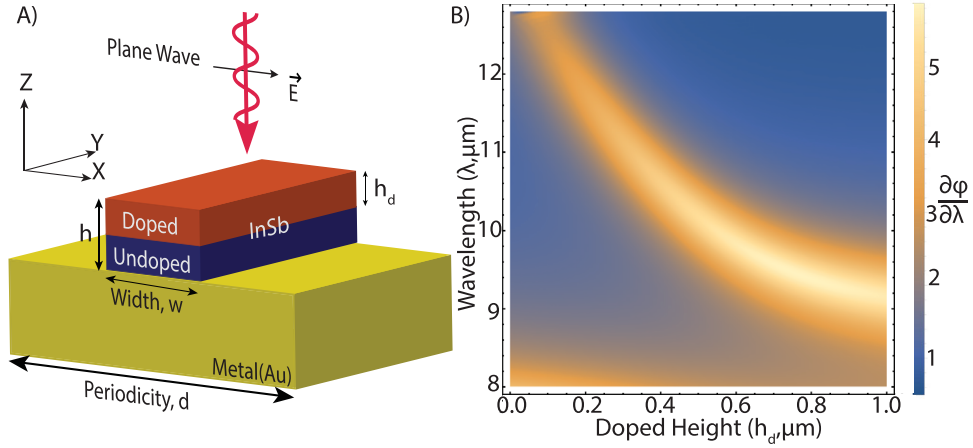

Figure 2. A) Sketch showing a resonator structure, where the topmost portion of the resonator (h_d) supports a large electron density (1.5×10^{18} cm^{-3}). B) Plot of the phase gradient showing the variation in resonance wavelength for a 1 μm tall (h) resonator as a function of the height of the doped InSb region, h_d . The resonance wavelength is most sensitive to changes in the carrier density within the top half of the resonator.

spherical InSb Mie resonators[36] showed that the index change ($\Delta n \approx 2$ based on Drude model) from a doping concentration of 1.5×10^{18} cm^{-3} was sufficient to obtain 2π phase shifts. We use a worst-case Drude scattering rate of 2 THz, reported for highly doped InSb,[32] for all carrier densities. Thus, we consider arrays of fixed-height InSb resonators comprising a high-carrier region (n-type: 1.5×10^{18} cm^{-3}) sitting atop an intrinsic region (**Figure 2**A). The dispersion of λ_{MD} as a function of the fractional height of the high-carrier region is shown in Figure 2B. When $h_d = 0$, we have a completely undoped resonator and when $h_d = h$ (total height of 1 μm) we have a completely doped resonator. λ_{MD} shifts from 13.5 to 9 μm as the resonator is changed from completely intrinsic InSb to completely high carrier concentration InSb. This shift in resonance wavelength happens primarily as the top 40% of the resonator carrier concentration is changed, as expected from the higher field concentrations in this region. Thus, our subsequent device design will focus on changing the carrier concentration only in this region. Additionally, any carrier-tunable device design will also require integrating a top electrode.

Our novel electrode design also takes advantage of the localization of electric fields within the top-middle portion of the resonator. Covering the resonator completely with a metal electrode eliminates the dielectric resonance (Supporting Information). A metal contact with a slit running down the center (**Figure 3**A), on the other hand, minimizes overlap of the metal electrode with the mode profile. Consider the case of a top Au electrode with a 1 μm gap. Although the electric fields are locally enhanced near the contacts, the magnetic field intensity is nearly identical to the original resonator. As a result, the reflection amplitude and phase (Figure 3C) are barely perturbed by the electrodes. The dispersion of resonance wavelengths with slit widths is further elaborated in Figure 3D. For a constant resonator size ($w = 3$ μm, $h = 1$ μm), the resonance wavelength can be shifted over a broadband region in the mid-infrared (8–18 μm). The gapped electrode resonator behaves like a split-dipole antenna[45] coupled to a dielectric resonator, enabling further engineering of resonance properties by exploiting narrow slits. Here, however, we consider slit widths of 1 μm, in which the resonance properties are very weakly perturbed. This forms the basis for our resonator platform, which includes top and bottom contacts with an index tunable semiconductor confining the optical mode.

Building from this basic resonator geometry, we integrate a device structure capable of modulating the electron concentration in the top 500 nm from 10^{16}–10^{18} cm^{-3}. The central challenge of designing such a device is the need to modulate large carrier densities over hundreds of nanometers. In a depletion mode device, for instance, the top of the resonator would be n-doped and the electrons pushed toward the bottom of the resonator with an applied voltage. However, the fundamental scaling of depletion width (W) versus applied voltage (V) and doping concentration (N) preclude this approach $W = \sqrt{\frac{2\varepsilon_0 \varepsilon_\infty V}{Nq}}$. To deplete an electron density of 2×10^{18} cm^{-3} from the top 400 nm would require over 185 V. To avoid this fundamental tradeoff, we design a device structure capable of generating large electron densities through carrier injection under forward bias. Simple p–n homojunctions are incapable of achieving the requisite carrier modulations and hence we turn instead to heterojunction designs adapted from existing light-emitting diodes (LEDs) and laser devices.[46–48]

Our heterojunction structure comprises aintrinsic InSb (470 nm) active region stacked between thin (30 nm) electron and hole blocking layers made of p-type and n-type $In_{0.8}Al_{0.2}Sb$ (lattice matched), respectively (**Figure 4**A). The device stack is completed by a p-type (10^{18} cm^{-3}) InSb hole source. Since the effective mass of holes in InSb ($m_h = 0.43\ m_0$) is much higher than electrons ($m_e = 0.014\ m_0$), the relevant index shifts arise from accumulating electrons in the topmost InSb layer. The device band structure is calculated via a 2D commercial device simulator[49] and shown in Figure 4B. Under forward bias electrons are injected from the top electrode into the active region, where they subsequently encounter the p-type $In_{0.8}Al_{0.2}Sb$ (1×10^{18} cm^{-3}) electron blocking layer. Holes are injected from the p-type InSb (5×10^{18} cm^{-3}) into the active region where they subsequently encounter the n-type

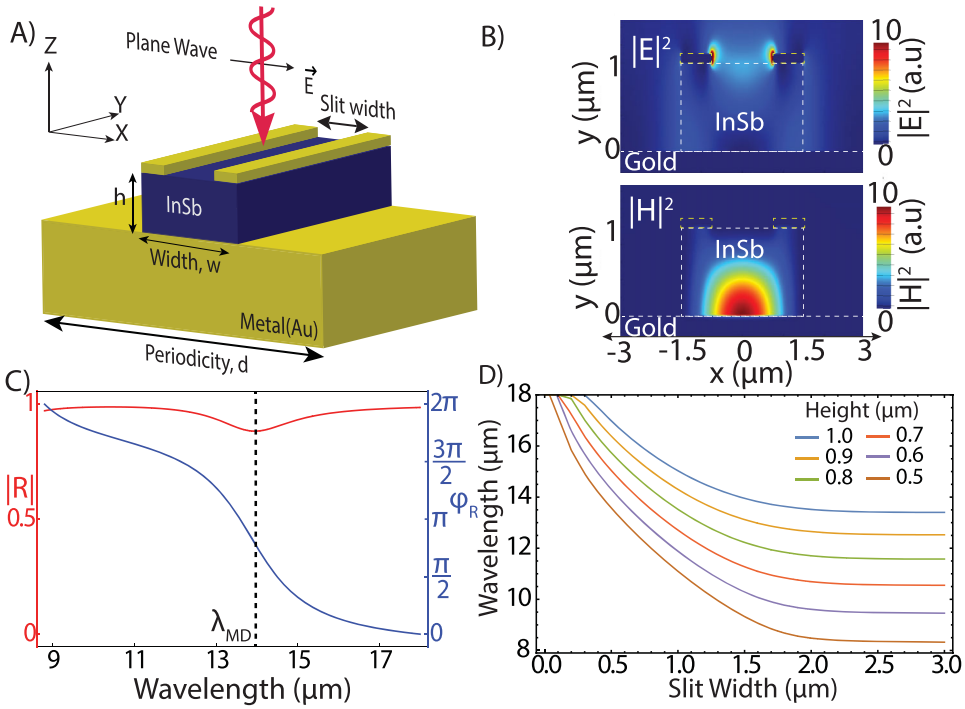

Figure 3. A) A resonator schematic showing the integration of a top electric contact with a central slit. B) Electric (top) and magnetic (bottom) field profiles of the fundamental magnetic dipole resonance excited within the resonator ($w = 3$ μm, $h = 1$ μm, $S_w = 1.5$ μm, and $d = 6$ μm) structure at an incident wavelength of 14 μm. Although the electric field intensity is enhanced near the electrode edges, the magnetic field intensity is only weakly perturbed by the introduction of the electrodes (compare to Figure 1B). C) Reflection amplitude (red axis on left) and phase (blue axis on right) as a function of the incident wavelength. The dashed line indicates the resonant wavelength $\lambda_{MD} = 14$ μm. The electrodes introduce a weak perturbation to the resonance wavelength. D) The resonant wavelength of the metal slit resonator as a function of slit width (S_w) and height (h). The resonator exhibits more significant shifts of the fundamental magnetic dipole resonance for narrow slit widths. For widths beyond 1.5 μm, the wavelength is only weakly perturbed.

$In_{0.8}Al_{0.2}Sb$ (1×10^{18} cm^{-3}) hole blocking layer. Electrons thus accumulate at high densities until they recombine with injected holes via band-to-band tunneling, Shockley–Read–Hall,[48] or Auger[50,51] processes. In the i-InSb layer, we assume an electron mobility[52] of 7000 cm^2 V^{-1} s^{-1} (400 cm^2 V^{-1} s^{-1} for holes). At all voltages, we assume an Auger-limited lifetime of 135 ps, a value consistent with studies of optically pumped InSb.[51,53] We use worst-case values of reported carrier lifetimes[53–56] and mobilities[52,57,58] at high carrier concentrations to identify phenomena that do not rely on optimistic input parameters. These recombination processes enable high-speed GHz operation (subject to suitable RC time constants) in the high injection forward bias scheme.[51,59] I–V curves under forward bias are calculated via 2D device simulation using the split top electrodes and plotted in Figure 4C. The electron density in the i-InSb active region (red curve) is uniformly (Figures S3 and S4, Supporting Information) modulated from 10^{17} to 3.5×10^{18} cm^{-3} by changing the forward bias from 0 to 1 V.

Combining these device simulations with electromagnetic FDTD simulations,[37] we extract the reflection phase and amplitude of an infinite metasurface array as a function of the applied voltage (Figure 4D). At an operation wavelength of 11.35 μm (center of the atmospheric transmission window[60,61]) a continuous reflection phase shift of 300° is obtained with less than 1.5 dB of loss as the applied voltage is varied between 0 to 0.9 V. Small kinks in the reflection amplitude ($0.55 < V < 0.75$, Figure 4D) arise from simulation artifacts caused by a "lightning rod" effect wherein fields are concentrated at perfectly right angle edges and corners (Figure S5, Supporting Information). These results demonstrate an almost 2π phase shift with minimal losses in amplitude. The difference of 60 degrees from the maximum of 2π possible phase shift is due to the lack of confinement of the radiating mode within the index tunable active region. As we will show subsequently, this range of phase tunability is sufficient to reliably dial in arbitrary phase profiles. Thus, these device resonators form the basic element of a reconfigurable metasurface capable of performing the function of virtually any linear diffractive or refractive optical element.

To illustrate the reconfigurable capability of such tunable metasurfaces, we demonstrate a voltage controlled mid-infrared beam deflector. A beam steering device requires imparting a constant phase gradient $\left(\frac{\partial\varphi}{\partial x}\right)$ across a metasurface. The diffracted angle is given by a grating equation[62] $\sin\theta_r = \sin\theta_i + \frac{\lambda}{2\pi}\frac{\partial\varphi}{\partial x}$, where θ_r is the angle of diffraction, θ_i is the angle of incidence ($\theta_i = 0$, at normal incidence), λ is the operating wavelength, and $\frac{\partial\varphi}{\partial x}$ is the spatial phase gradient. Based on Figure 4C, we can map the required phase gradient on the metasurface by applying the appropriate periodic voltage profile across an array of otherwise uniform tunable

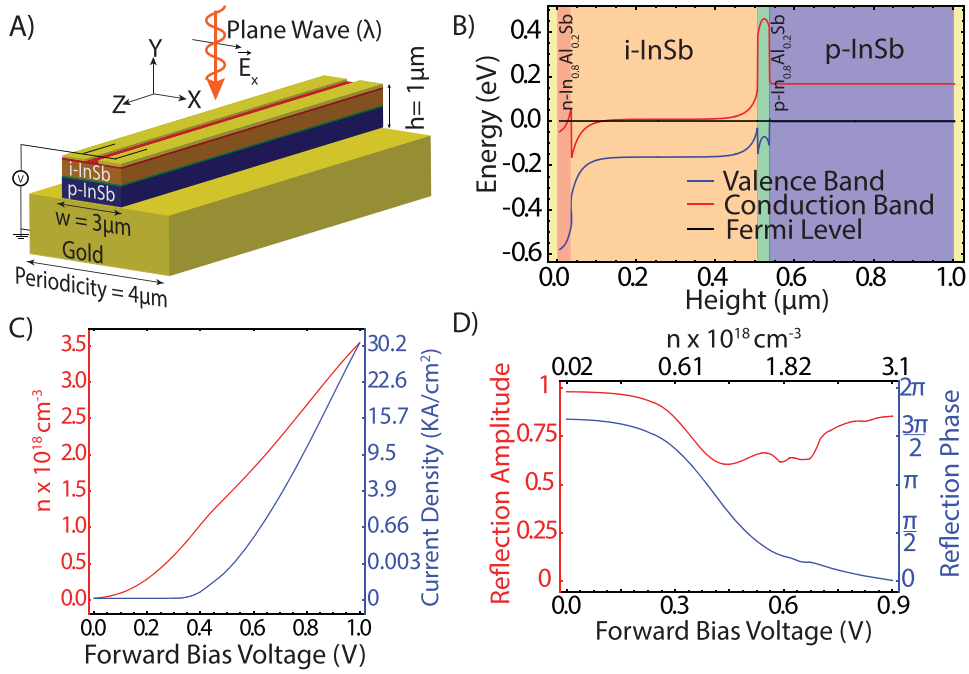

Figure 4. A) Sketch of the heterojunction p-($InSb/In_{0.8}Al_{0.2}Sb$):i-InSb:n-$In_{0.8}Al_{0.2}Sb$ junction resonator structure of width w = 3 μm, height h = 1 μm (h_{i-InSb} = 0.47 μm +h_{p-InSb} = 0.47 μm +$h_{p-InAlSb}$ = 0.03 μm +$h_{n-InAlSb}$ = 0.03 μm), metal slit width S_w = 1 μm, and periodicity d = 4 μm, operating under forward bias V. B) Band diagram of the resonator showing the band alignments of the type-II staggered heterojunction with both electron (≈0.4 eV) and hole (≈0.3 eV) barriers at 0 V of applied bias. C) Forward bias device characteristics of the hetero p–n junction device showing the current density (blue, right axis) and the electron concentration (red, left axis) inside i-InSb as a function of the applied forward bias V. The InSb accumulates a large electron density with less than a volt of applied bias. D) Voltage-dependent reflection characteristics of a periodic array of resonators (Figure 4A) at an operating wavelength of 11.35 μm. The red curve (left axis) shows the reflection amplitude ($|S_{11}|^2$) and the blue curve (right axis) shows the reflection phase (Arg (S_{11})) as a function of charge carrier concentration inside InSb (bottom axis) and the applied forward bias (top axis). The phase varies by nearly 2π with less than a volt of applied bias.

resonators. To start, we consider the simplest cases where the phase shift between adjacent resonators is an integer fraction of 2π (**Figure 5**A). In such cases the linear phase gradient is given by $\frac{\partial\varphi}{\partial x}=\frac{2\pi}{\Lambda_{\text{eff}}}$, where $\Lambda_{\text{eff}}=n\times d$, d is the inter-resonator spacing, and n is the integer number of resonators over which the voltage profile repeats itself. Hence the diffraction angle is given by $\sin\theta_r=\frac{\lambda}{\Lambda_{\text{eff}}}$, the standard equation for a beam deflector in diffractive optics.[63]

The wavelength and angle dependent diffraction for an array of resonators (w = 3 μm, h = 1 μm and d = 4 μm), with n = 5 (inter-resonar phase shift of 72°) is shown in Figure 5B. The incident plane wave couples only to the +1 diffraction grating mode at 34.5° at an operation wavelength of 11.35 μm. The broadband nature of the magnetic dipole resonance (low Q) ensures a roughly 2 μm (Half Power Beam Width of the +1 diffraction lobe from 10 to 12 μm) spectral bandwidth for this diffraction lobe. The array exhibits a high diffraction efficiency; more than 60% of the incident light is diffracted into the desired direction. The scattering efficiency is even higher; more than 85% percent of the total reflected light is directed into the desired diffraction lobe. This diffraction lobe is plotted as the green curve in Figure 5C. As can be inferred from this figure, changing the periodicity of the applied voltage profile enables nearly 180° tuning of the desired diffraction lobe.

The maximal asymmetric angle of deflection for an integer periodic structure is given by n = 3, corresponding to an angle of 72°. As expected from the properties of diffraction gratings,[63] high reflection angles exhibit lower diffraction efficiency than smaller reflection angles since a greater fraction of the resonators are tuned to a lossy state. As the integer periodicity increases, the diffracted lobe moves toward the normal and quickly increases in efficiency. For periodicities of 5 or greater (green), the diffraction and scattering efficiencies are basically constant. Although we only show easily simulated cases where the phase is 2π periodic with n resonators, any intermediate diffraction angle can also be achieved by dialing in the appropriate, not necessarily periodic phase profile. However, in these cases phase errors are introduced whenever the necessary resonator phase is between 300° and 360°—values inaccessible in our voltage-controlled scheme (Figure 4D). To determine the impact of these phase errors, we consider a worst-case scenario corresponding to an integer repeat of n = 12. In this case, the 11th resonator element should have a reflection phase of 330°. Since the phase can only be specified as either 300° or 360° (i.e., 0°), this introduces a maximal phase error of ±30°. Despite this repeating phase error, the array still exhibits a high quality diffraction lobe, with diffraction efficiency nearly identical to the alternate cases with zero phase error. Thus, these results

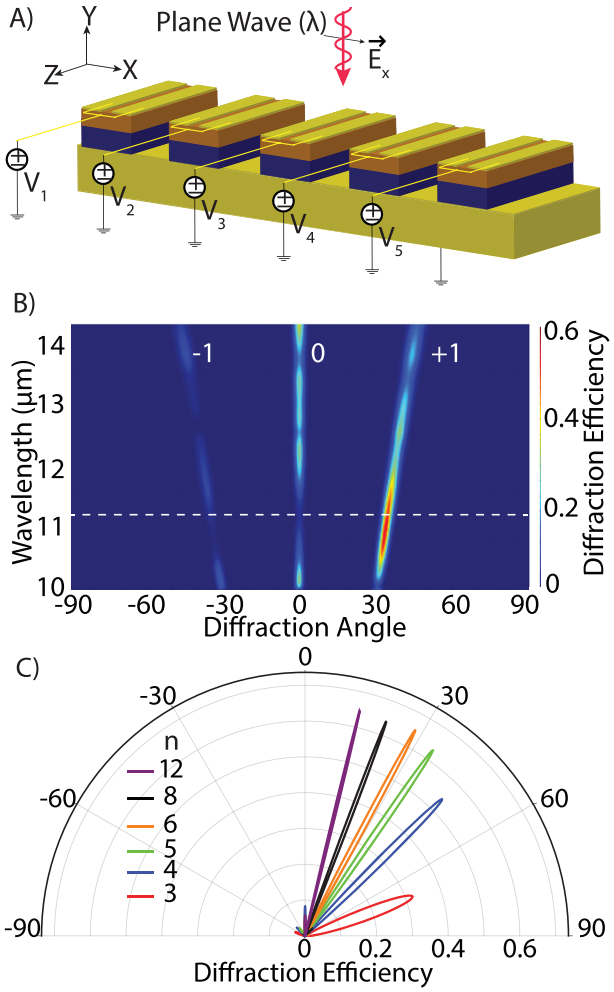

Figure 5. A) A metasurface with a periodic potential (V_{1-5}; $V_6 = V_1$) forms a spatial phase gradient ($\frac{\partial\varphi}{\partial x} = 2\pi/5d = \pi/10$ μm) based on periodicity ($5d$) of the applied bias. B) The normalized reflected field amplitude is plotted as a function of the incident wavelength and the diffraction angle. The spatial phase gradient induces a high quality unidirectional diffraction lobe (marked +1) at an operating wavelength of 11.35 μm (dashed white line). The spectral bandwidth of this lobe is 2 μm. C) Polar plots showing the directional diffraction lobes of the reflected beam at 11.35 μm for different voltage-dependent spatial phase gradients ($\frac{\partial\varphi}{\partial x} = \frac{2\pi}{n.d}$; $n = 3$, 4, 5, 6, 8, & 12) for a linearly polarized plane wave at normal incidence. The case of $n = 12$ (purple) corresponds to the maximal possible phase error of the device. The metasurface enables continuous tuning of high quality diffraction lobes over a large angular range.

demonstrate metasurfaces capable of continuous and reconfigurable beam steering over a large angular range with high efficiency.

3. Conclusions

In conclusion, we have shown that high-index heterojunction semiconductor resonators can serve as building blocks in phase tunable reflect-array metasurface devices. Such devices are anticipated to be reconfigurable at GHz time scales and capable of mimicking nearly all linear refractive and diffractive optical elements. Heterojunction devices using InSb and InAlSb layers, (infrared detectors,[55,64] LEDs,[65,66] transistors,[58,67,68] etc.) similar to the proposed structure have been demonstrated with comparable device characteristics. Fabrication issues related to dry etching and surface passivation[69,70] with thin layers of SiN_x (or other dielectrics), etc. have been successfully overcome to form state of the art devices using InSb and InAlSb layers. These metasurface resonators exploit novel lattice matched InSb-based devices to electrically modulate free-carrier densities over a large range and volume. The index tunable active layer is designed to maximally overlap with the high electric field concentration of a resonant magnetic dipole mode. We demonstrate a continuously tunable phase shift of 300° with less than 1 dB loss at 11.35 μm with a voltage swing of less than 1 V. As an illustration of this tunable performance, we demonstrate a highly efficient beam steering reflect-array device. This reconfigurable metasurface exhibits high diffraction and scattering efficiencies over a nearly 180° (±90°) field of view. This demonstration highlights the potential of reconfigurable metasurfaces, and suggests the possibility of creating metasurface-enable infrared optics reconfigurable at GHz frequencies.

Supporting Information

Supporting Information is available from the Wiley Online Library or from the author.

Acknowledgements

P.P.I. and J.A.S. proposed and conceived the idea. P.P.I. performed the numerical device and electromagnetic simulations. M.P. helped P.P.I. to design the heterostructure device design. P.P.I. and J.A.S. analyzed the data and wrote the manuscript. The authors would like to thank Prof. Chris Palmstrom for his useful insights during the course of this work. This work was supported from the Air Force Office of Scientific Research Young Investigator Program (Grant No. FA9550-13-1-0182). The authors also acknowledge support from the Centre for Scientific Computing from the CNSI, MRL: an NSF MRSEC (DMR-1121053) & NSF CNS-0960316.

Received: April 21, 2016
Revised: May 24, 2016
Published online: July 4, 2016

[1] S. Jahani, Z. Jacob, *Nat. Nanotechnol.* **2016**, *11*, 23.
[2] N. I. Zheludev, Y. S. Kivshar, *Nat. Mater.* **2012**, *11*, 917.
[3] A. V Kildishev, A. Boltasseva, V. M. Shalaev, *Science* **2013**, *339*, 1232009.
[4] N. Yu, F. Capasso, *Nat. Mater.* **2014**, *13*, 139.
[5] N. I. Zheludev, E. Plum, *Nat. Nanotechnol.* **2016**, *11*, 16.
[6] A. Arbabi, Y. Horie, M. Bagheri, A. Faraon, *Nat. Nanotechnol.* **2015**, *10*, 937.
[7] D. Fattal, J. Li, Z. Peng, M. Fiorentino, R. G. Beausoleil, *Nat. Photonics* **2010**, *4*, 466.
[8] Y. Yao, R. Shankar, M. Kats, Y. Song, J. Kong, M. Loncar, F. Capasso, *Nano Lett.* **2014**, *14*, 6526.
[9] C. Argyropoulos, *Opt. Express* **2015**, *23*, 23787.

[10] Y. Yang, W. Wang, P. Moitra, I. I. Kravchenko, D. P. Briggs, J. Valentine, *Nano Lett.* **2014**, *14*, 1394.
[11] N. K. Grady, J. E. Heyes, D. R. Chowdhury, Y. Zeng, M. T. Reiten, A. K. Azad, A. J. Taylor, D. A. R. Dalvit, H.-T. Chen, *Science* **2013**, *340*, 1304.
[12] J. W. Goodman, *Introduction to Fourier Optics*, Roberts And Company Publishers, Englewood, CO, USA **2005**.
[13] P. R. West, J. L. Stewart, A. V. Kildishev, V. M. Shalaev, V. V. Shkunov, F. Strohkendl, Y. A. Zakharenkov, R. K. Dodds, R. Byren, *Opt. Express* **2014**, *22*, 26212.
[14] J. A. Schuller, E. S. Barnard, W. Cai, Y. C. Jun, J. S. White, M. L. Brongersma, *Nat. Mater.* **2010**, *9*, 193.
[15] S. J. Kim, P. Fan, J.-H. Kang, M. L. Brongersma, *Nat. Commun.* **2015**, *6*, 7591.
[16] S. A. Mann, R. R. Grote, R. M. Osgood, J. A. Schuller, *Opt. Express* **2011**, *19*, 25729.
[17] L. Cao, P. Fan, A. P. Vasudev, J. S. White, Z. Yu, W. Cai, J. A. Schuller, S. Fan, M. L. Brongersma, *Nano Lett.* **2010**, *10*, 439.
[18] Y. Yang, I. I. Kravchenko, D. P. Briggs, J. Valentine, *Nat. Commun.* **2014**, *5*, 5753.
[19] B. Luk'yanchuk, N. I. Zheludev, S. A. Maier, N. J. Halas, P. Nordlander, H. Giessen, C. T. Chong, *Nat. Mater.* **2010**, *9*, 707.
[20] D. K. Gramotnev, S. I. Bozhevolnyi, *Nat. Photonics* **2010**, *4*, 83.
[21] C. Pfeiffer, N. K. Emani, A. M. Shaltout, A. Boltasseva, V. M. Shalaev, A. Grbic, *Nano Lett.* **2014**, *14*, 2491.
[22] M. Decker, I. Staude, M. Falkner, J. Dominguez, D. N. Neshev, I. Brener, T. Pertsch, Y. S. Kivshar, *Adv. Opt. Mater.* **2015**, *3*, 813,
[23] J. Lee, S. Jung, P.-Y. Chen, F. Lu, F. Demmerle, G. Boehm, M.-C. Amann, A. Alù, M. A. Belkin, *Adv. Opt. Mater.* **2014**, *2*, 1057.
[24] V. W. Brar, M. C. Sherrott, M. S. Jang, S. Kim, L. Kim, M. Choi, L. A. Sweatlock, H. A. Atwater, *Nat. Commun.* **2015**, *6*, 7032.
[25] Y. C. Jun, I. Brener, *J. Opt.* **2012**, *14*, 114013.
[26] T. Taliercio, V. Ntsame Guilengui, L. Cerutti, J. B. Rodriguez, F. Barho, M. J. M Rodrigo, F. Gonzalez-Posada, E. Tournié, M. Niehle, A. Trampert, *Opt. Expess*, **2015**, *23*, 29423.
[27] S. Law, C. Roberts, T. Kilpatrick, L. Yu, T. Ribaudo, E. A. A. Shaner, V. Podolskiy, D. Wasserman, *Phys. Rev. Lett.* **2014**, *112*, 17401.
[28] K. Anglin, T. Ribaudo, D. C. Adams, X. Qian, W. D. Goodhue, S. Dooley, E. A. Shaner, D. Wasserman, *J. Appl. Phys.* **2011**, *109*, 123103.
[29] B. Lee, J. Park, G.-H. Han, H.-S. Ee, C. H. Naylor, W. Liu, A. T. C. Johnson, R. Agarwal, *Nano Lett.*, **2015**, *15*, 3646.
[30] H.-S. Ee, R. Agarwal, *Nano Lett.* **2016**, *16*, 2818.
[31] P. P. Paskov, L. I. Pavlov, *Appl. Phys. B Photophys. Laser Chem.* **1992**, *54*, 113.
[32] S. Law, R. Liu, D. Wasserman, *J. Vac. Sci. Technol. B Nanotechnol. Microelectron. Mater. Process. Meas. Phenom.* **2014**, *32*, 52601.
[33] B. S. Passmore, D. G. Allen, S. R. Vangala, W. D. Goodhue, D. Wasserman, E. A. Shaner, *Opt. Express* **2009**, *17*, 10223.
[34] T. P. Steinbusch, H. K. Tyagi, M. C. Schaafsma, G. Georgiou, J. Gómez Rivas, *Opt. Express* **2014**, *22*, 26559.
[35] S. Law, D. C. Adams, A. M. M. Taylor, D. Wasserman, *Opt. Express* **2012**, *20*, 12155.
[36] P. P. Iyer, N. A. Butakov, J. A. Schuller, *ACS Photonics* **2015**, *2*, 1077.
[37] FDTD Solutions, www.lumerical.com, (accessed: December 2015).
[38] C. F. Bohren, D. R. Huffman, *Absorption and Scattering of Light by Small Particles*, Wiley, Weinheim, Germany **2008**.
[39] H. C. Hulst, H. C. van de Hulst, *Light Scattering by Small Particles*, Courier Corporation, New York **1957**.
[40] J. Lin, L. Huang, Y. Yu, S. He, L. Cao, *Opt. Express* **2015**, *23*, 19154.
[41] F. Aieta, M. A. Kats, P. Genevet, F. Capasso, *Science* **2015**, *347*, 1342.
[42] M. Khorasaninejad, F. Aieta, P. Kanhaiya, M. A. Kats, P. Genevet, D. Rousso, F. Capasso, *Nano Lett.* **2015**, *15*, 5358.
[43] J. A. Schuller, M. L. Brongersma, *Opt. Express* **2009**, *17*, 24084.
[44] E. Xifré-Pérez, L. Shi, U. Tuzer, R. Fenollosa, F. Ramiro-Manzano, R. Quidant, F. Meseguer, *ACS Nano* **2013**, *7*, 664.
[45] N. A. Butakov, J. A. Schuller, *Opt. Express* **2015**, *23*, 29698.
[46] A. A. Allerman, R. M. Biefeld, S. R. Kurtz, *Appl. Phys. Lett.* **1996**, *69*, 465.
[47] A. Krier, *Mid-Infrared Semiconductor Optoelectronics*, Springer, London, UK **2006**.
[48] T. Ashley, *Philos. Trans. R. Soc. A Math. Phys. Eng. Sci.* **2001**, *359*, 475.
[49] ATLAS, www.silvaco.com, (accessed: May 2016).
[50] Y. Aytac, B. V. Olson, J. K. Kim, E. A. Shaner, S. D. Hawkins, J. F. Klem, M. E. Flatté, T. F. Boggess, *J. Appl. Phys.* **2015**, *118*, 125701.
[51] V. Chazapis, H. A. Blom, K. L. Vodopyanov, A. G. Norman, C. C. Phillips, *Phys. Rev. B* **1995**, *52*, 2516.
[52] E. Litwin-Staszewska, W. Szyma ska, R. Piotrzkowski, *Phys. Status Solidi* **1981**, *106*, 551.
[53] B. N. Murdin, M. Kamal-Saadi, A. Lindsay, E. P. O'Reilly, A. R. Adams, G. J. Nott, J. G. Crowder, C. R. Pidgeon, I. V. Bradley, J.-P. R. Wells, T. Burke, A. D. Johnson, T. Ashley, *Appl. Phys. Lett.* **2001**, *78*, 1568.
[54] V. Chazapis, H. A. Blom, K. L. Vodopyanov, A. G. Norman, C. C. Phillips, *Phys. Rev. B* **1995**, *52*, 2516.
[55] A. Evirgen, J. Abautret, J. P. Perez, H. Aït-Kaci, P. Christol, J. Fleury, H. Sik, A. Nedelcu, R. Cluzel, A. Cordat, *Proc. SPIE* **2014**, *8993*, 899313.
[56] T. Fishman, V. Nahum, E. Saguy, Z. Calahorra, I. Shtrichman, *Proc. SPIE* **2007**, *6660*, 666005.
[57] A. J. Strauss, *J. Appl. Phys.* **1959**, *30*, 559.
[58] W. K. Liu, *J. Vac. Sci. Technol., B: Microelectron. Nanometer Struct.* **1996**, *14*, 2339.
[59] R. D. Thom, T. L. Koch, J. D. Langan, W. J. Parrish, *IEEE Trans. Electron Dev.* **1980**, *27*, 160.
[60] I. S. Glass, *Handbook of Infrared Astronomy/I.S. Glass Cambridge*, Vol. *1*, Cambridge University Press, New York **1999**.
[61] S. D. Lord, *A New Software Tool for Computing Earth's Atmospheric Transmission Near- and Far-infrared Radiation, NASA Technical Memorandum (1039)*, USA, **1992**.
[62] N. Yu, P. Genevet, M. A. Kats, F. Aieta, J.-P. Tetienne, F. Capasso, Z. Gaburro, *Science* **2011**, *334*, 333.
[63] E. G. Loewen, E. Popov, *Diffraction Gratings and Applications*, Marcel Dekker, Inc., New York **1997**.
[64] J.-P. Perez, A. Evirgen, J. Abautret, P. Christol, A. Cordat, A. Nedelcu, *Proc. SPIE* **2015**, *9370*, 93700N.
[65] T. Ashley, C. T. Elliott, N. T. Gordon, R. S. Hall, A. D. Johnson, G. J. Pryce, *Appl. Phys. Lett.* **1994**, *64*, 2433.
[66] K. Ueno, E. G. Camargo, T. Morishita, Y. Moriyasu, H. Goto, N. Kuze, *J. Cryst. Growth* **2011**, *323*, 463.
[67] J. M. S. Orr, P. D. Buckle, M. Fearn, C. J. Storey, L. Buckle, T. Ashley, *New J. Phys.* **2007**, *9*, 261.
[68] S. Datta, *Microelectron. Eng.* **2007**, *84*, 2133.
[69] S. Yumrukçu, *Master Thesis*, Bilkent University, Ankara, Turkey, **2010**.
[70] H. Simchi, G. Sareminia, A. Shafiekhani, G. Valizadeh, *Infrared Phys. Technol.* **2008**, *51*, 263.